ACS NANO
Cite This: ACS Nano 2019, 13, 13027−13036
www.acsnano.org

ARTICLE

Spill-SOS: Self-Pumping Siphon-Capillary Oil Recovery

Shenghao Wu,[†,#] Huachao Yang,[†,#] Guoping Xiong,[§,#] Yikuan Tian,[†] Biyao Gong,[†] Tengfei Luo,[‡] Timothy S. Fisher,[∥] Jianhua Yan,[†] Kefa Cen,[†] Zheng Bo,[*,†] and Kostya Ken Ostrikov[†,▽,⊥]

[†]State Key Laboratory of Clean Energy Utilization, College of Energy Engineering, Zhejiang University, Hangzhou, Zhejiang 310027, China

[§]Department of Mechanical Engineering, University of Nevada, Reno, Nevada 89557, United States

[‡]Department of Aerospace and Mechanical Engineering, University of Notre Dame, Notre Dame, Indiana 46556, United States

[∥]Department of Mechanical & Aerospace Engineering and California nanoSystems Institute, University of California, Los Angeles, California 90095, United States

[▽]School of Chemistry, Physics and Mechanical Engineering, Queensland University of Technology, Brisbane, Queensland 4000, Australia

[⊥]Joint CSIRO-QUT Sustainable Processes and Devices Laboratory, P.O. Box 218, Lindfield, New South Wales 2070, Australia

Supporting Information

ABSTRACT: **Oil spills remain a worldwide challenge and need emergency "spill-SOS" actions when they occur. Conventional methods suffer from complex processes and high cost. Here, we demonstrate a solar-heating siphon-capillary oil skimmer (S-SOS) that harvests solar energy, gravitational potential energy, and solid surface energy to enable efficient oil spill recovery in a self-pumping manner. The S-SOS is assembled by an inverted U-shape porous architecture combining solar-heating, siphon, and capillary effects, and works without any external power or manual interventions. Importantly, solid surface energy is used by capillary adsorption to enable the self-starting behavior, gravitational potential energy is utilized by siphon transport to drive the oil flow, and solar energy is harvested by solar-thermal conversion to facilitate the transport speed. In the proof-of-concept work, an all-carbon hierarchical architecture (VG/GF) is fabricated by growing vertically oriented graphene nanosheets (VGs) on a monolith of graphite felt (GF) via a plasma-enhanced method to serve as the U-shape architecture. Consequently, an oil-recovery rate of 35.2 L m^{-2} h^{-1} is obtained at ambient condition. When exposed to normal solar irradiation, the oil-recovery rate dramatically increases to 123.3 L m^{-2} h^{-1}. Meanwhile, the solar-thermal energy efficiency is calculated to be 75.3%. Moreover, the S-SOS system presents excellent stability without obvious performance-degradation over 60 h. The outstanding performance is ascribed to the enhanced siphon action, capillary action, photonic absorption, and interfacial heating in the plasma-made graphene nanostructures. Multiple merits make the current S-SOS design and the VG/GF nanostructures promising for efficient oil recovery and transport of energy stored in chemical bonds.**

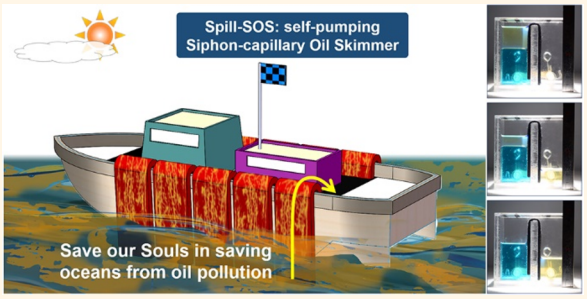

KEYWORDS: *oil recovery, siphon and capillary actions, solar-thermal conversion, plasma-made nanostructures, fluid transport*

With the fast development of marine oil exploitation and transportation, increased oil spill accidents have not only caused severe and long-term damage to aquatic ecosystems, but also led to a great loss of valuable resources.[1−3] To remedy the oil spills and save the energy, energy-efficient and environment-friendly oil recovery methods (*i.e.*, "spill-SOS" actions) are highly desired. Currently, the commonly used technologies for oil spill remediation include oil containment booms, skimmer vessels, *in situ* combustion, physical diffusion, enhanced bioremediation, and physical adsorption by oil-sorption materials.[4−6] Among these technologies, physical adsorption by porous hydrophobic and oleophilic materials (*i.e.*, capillary adsorption, see the schematic in Figure S1b) attracted increasing attention due to the *in situ* collection of oil from a water surface.[4] Although the adsorbed oil can be recycled by post-treatments such as squeezing and pumping,[7−14] the sophisticated and multistep procedures require complex devices (e.g., pump, squeezer, and heater)

Received: July 20, 2019
Accepted: October 29, 2019
Published: October 29, 2019

DOI: 10.1021/acsnano.9b05703
ACS Nano 2019, 13, 13027−13036

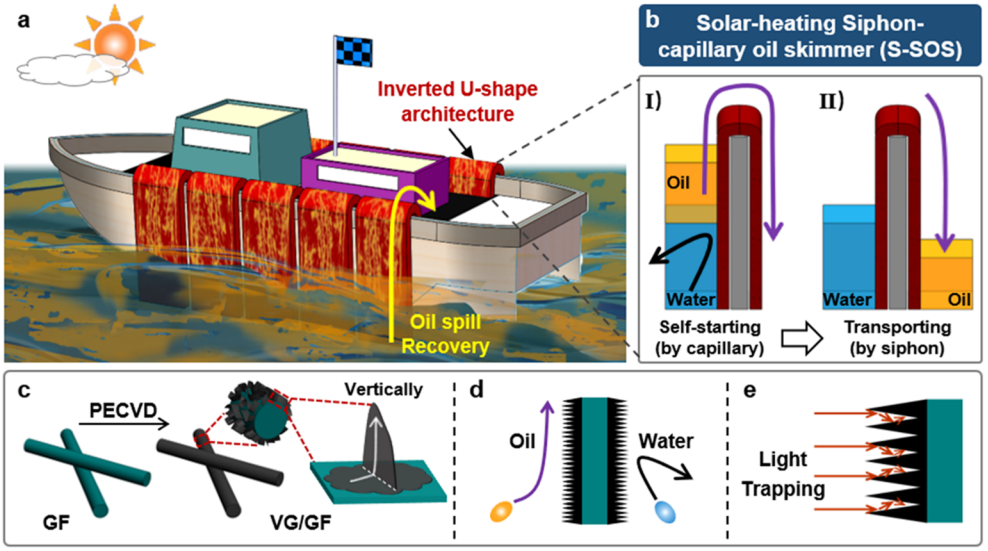

Figure 1. Schematic illustration of the solar-heating siphon-capillary oil skimmer (S-SOS). (a) The inverted U-shape architecture (red) is equipped on the gunnel of a marine vessel. Viscous oil (yellow) floats on the ocean (blue). The oil transports through the U-shape architecture into the vessel in a self-pumping manner and is then collected. (b) Illustration of the principal two steps: (I) self-starting by capillary adsorption, and (II) transporting oil by siphon action. (c–e) Three key features of the S-SOS design: porous structure (c); oleophilic and hydrophobic wettability (d); high photonic absorption (e).

and consume a large amount of energy during operation. To reduce the economic and energetic costs for oil recovery, improved strategies, especially without complex procedures and devices, need to be developed.

Siphon, a common phenomenon in nature, is capable of continuously transporting a liquid only driven by gravity without external input of power.[15] As such, it presents a possibility to enable an automatic unattended approach for fluid transport, including oil transport. Previously, siphon-based devices have been proposed for various applications, such as irrigation and spillway.[16−18] However, few studies are reported on utilizing siphon action for oil recovery,[19] not to mention the optimization and improvement of the siphon action for the oil recovery performance. Moreover, the previous siphon devices applied for fluid transport still suffer from two significant issues (Figure S1b), which deteriorate the performance in practical applications: (i) Poor stability and inability to self-restart. An automatic unattended device needs to be able to function reliably without failure and constant maintenance. However, the previous siphon devices often malfunction because of the air accumulation in the siphon conduits.[20,21] Meanwhile, it is unable to self-restart and requires manual interventions to return to normal flow operation after malfunction. Generally, an electricity-powered pump is equipped to help the siphon device restart, which increases the economic cost and energy consumption. (ii) Nonselectivity for fluid transport. A typical siphon device is often assembled by a conduit that serves as the transport channel. When working in a multiple-component liquid, as shown in Figure S1b, they are unable to choose which component to transport. On the other hand, the real-world liquid is often composed by two or more components.[22,23] Therefore, the traditional siphon devices fail to meet the complex conditions in practical applications. To achieve selective transport of oil by siphon action and separate the oil from water, further improvements are needed.

Herein, a solar-heating siphon-capillary oil skimmer (S-SOS) is proposed to harvest solar energy, gravitational potential energy, and surface energy to enable efficient oil spill cleanup and recycle the energy stored in chemical bonds (*i.e.*, oil) in a self-pumping manner. As schematically shown in Figure 1a,b, the S-SOS is assembled by an inverted U-shape porous architecture combining a solar-heating effect, siphon action, and capillary action. Importantly, the surface energy is used by capillary adsorption to enable the self-starting behavior, the gravitational potential energy is utilized by siphon transport to drive the oil flow, and the solar energy is harvested by solar-thermal conversion to facilitate the transport speed. The oil floating on the water surface flows through the U-shape architecture that covers a vertical wall and is then collected and stored while no external power or no manual intervention is used. More information describing the concept and operation is available in supporting section 2.

By growing vertically oriented graphene nanosheets (VGs) on a monolith of graphite felt (GF) through a one-step plasma-enhanced chemical vapor deposition (PECVD) process, an all-carbon hierarchical architecture (VG/GF) is fabricated to serve as the U-shape architecture. The as-obtained nanostructures lead to the enhanced siphon action, capillary action, photonic absorption, and interfacial heating, which eventually benefit the oil recovery performance. Consequently, an oil-recovery rate of 35.2 L m^{-2} h^{-1} is obtained at ambient condition. When exposed to a normal solar irradiation of 1 kW m^{-2}, the oil-recovery rate dramatically increases to 123.3 L m^{-2} h^{-1}. Meanwhile, the solar-thermal energy efficiency is calculated to be 75.3%. Moreover, the S-SOS system displays a long-term stability without obvious performance-degradation over 60 h.

RESULTS AND DISCUSSION

Key Features of the S-SOS Device. Three key features are required for the S-SOS, as shown in Figure 1c–e. (i) Porous structure (see Figure 1c). Since the siphon and capillary actions usually occur in porous structures, the U-shape architecture should be composed of porous materials. In

DOI: 10.1021/acsnano.9b05703
ACS Nano 2019, 13, 13027−13036

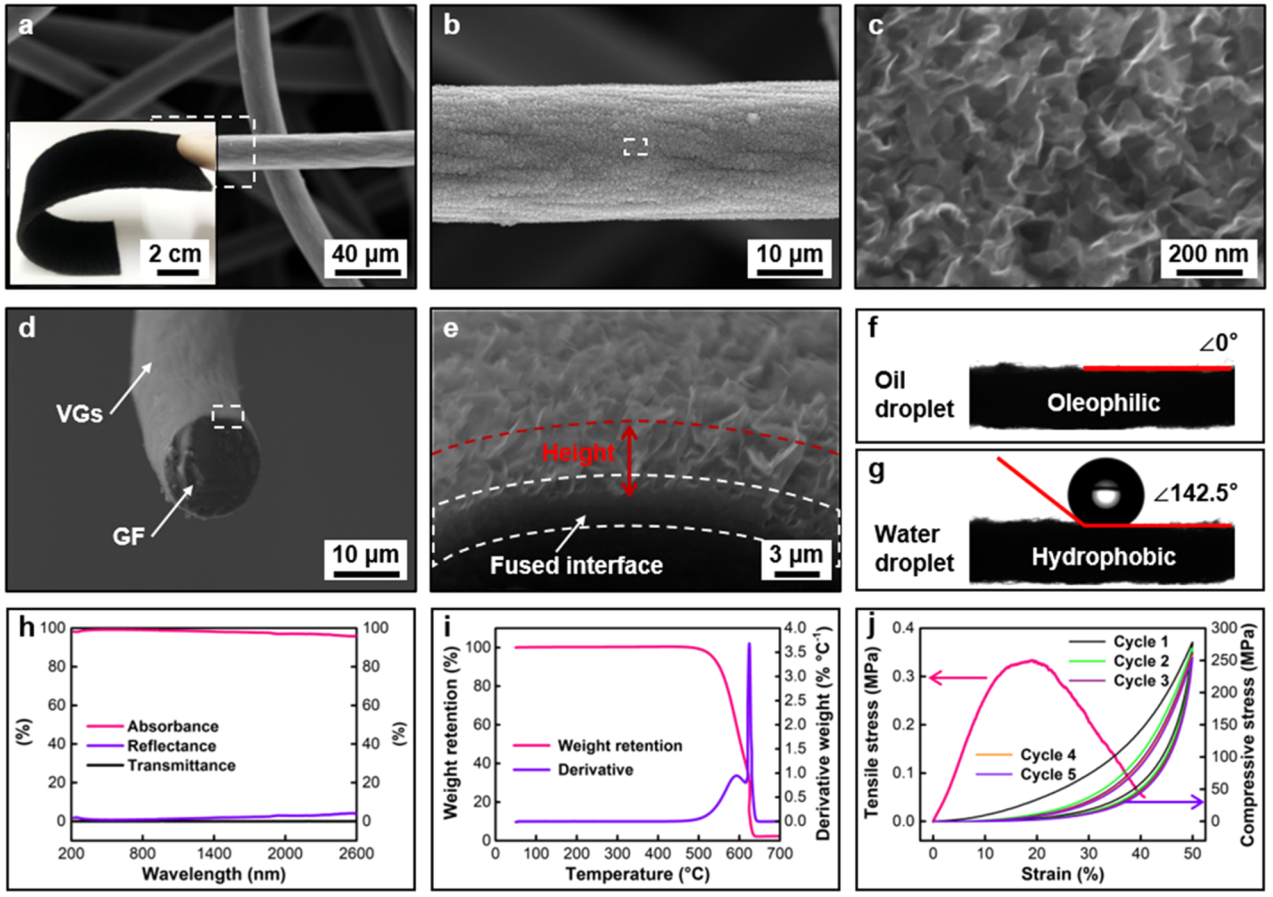

Figure 2. Structural characterization of the VG/GF sample. (a–c) Top-view SEM images of the VG/GF sample. Optical image of VG/GF in the inset of panel a. (d and e) Cross-sectional SEM images of VG/GF. (f) Oil contact angle of the VG/GF sample, suggesting a superoleophilic nature. (g) Water contact angle of the VG/GF sample, suggesting a superhydrophobic nature. (h) Photonic property of the VG/GF sample. The red curve represents absorbance. The purple curve represents reflectance. The black curve represents transmittance. (i) Thermogravimetric curve and derivative thermogravimetric curve of the VG/GF sample under the flow of O_2/N_2 (with a ratio of 1:4). (j) Mechanical behavior of the VG/GF sample. The red curve represents tensile performance, while the other curves represent the compressive performance.

the current proof-of-concept work, the U-shape architecture is fabricated by growing VGs on a GF monolith via a one-step PECVD process, obtaining a hierarchical porous architecture (denoted as VG/GF). (ii) Oleophilic and hydrophobic wettability (see Figure 1d). Surface wettability determines which liquid to absorb and then transport. The surface of the U-shape architecture should be oleophilic and meanwhile hydrophobic to separate oil from water. The all-carbon VG/GF with intrinsically oleophilic and hydrophobic wettability is applicable. (iii) High photonic absorption (see Figure 1e). Since a solar-heating effect is intentionally introduced to improve the oil transport behavior, a high photonic absorption is important to capture solar energy and then convert it to thermal energy. The plasma-made VGs present a vertical orientation, exposed edges, and a high density of nanoarrays, which is conducive for trapping light.

Material Characterization. An all-carbon hierarchical material (*i.e.*, VG/GF) is used as the inverted U-shape architecture. As shown in Figure S2, the pristine GF is composed of carbon fibers with porous structure, smooth surface, and gray color. Through the PECVD process, the wall-like VGs are uniformly coated on the carbon fibers of GF, leading to a rough surface, as shown in Figure 2a–c. Meanwhile, the porous hosting structure (*i.e.*, GF) is well-preserved after the VG growth process. The porosity of the VG/GF sample is measured to be 89.4%, which is very close to that of the pristine GF sample (90.4%). The as-obtained VG/GF sample changes the surface color to deep dark and maintains the initial flexibility (see the inset of Figure 2a). The VGs present high density graphene nanosheets, exposed edges, and open channels (see Figure 2c). The span of a single graphene nanosheet ranges from 100 to 300 nm. The side-view SEM images in Figure 2 panels d and e show that these VGs are perpendicularly ingrown from the cylindrical hosting structures (*i.e.*, carbon fibers) with a fused conjunction at the VG–GF interface. Such a fused conjunction is mechanically robust because it is connected by chemical bonds formed during chemical vapor deposition under an energy-intensive plasma sheath, as reported in our previous works.[24−26] More details on the plasma growth mechanism are available in supporting section 4. In addition, the typical thickness of the VGs is measured to be 1–5 μm (see Figure 2e). These graphene nanosheets with vertical orientation respective to the cylindrical substrate build up interconnected channels, which can serve as flow paths for fluid transport.

The surface wettability plays an important role in the ability of selective transport. The surface wettability of the VG/GF is measured and shown in Figure 2f,g. When an oil droplet is in

DOI: 10.1021/acsnano.9b05703
ACS Nano 2019, 13, 13027−13036

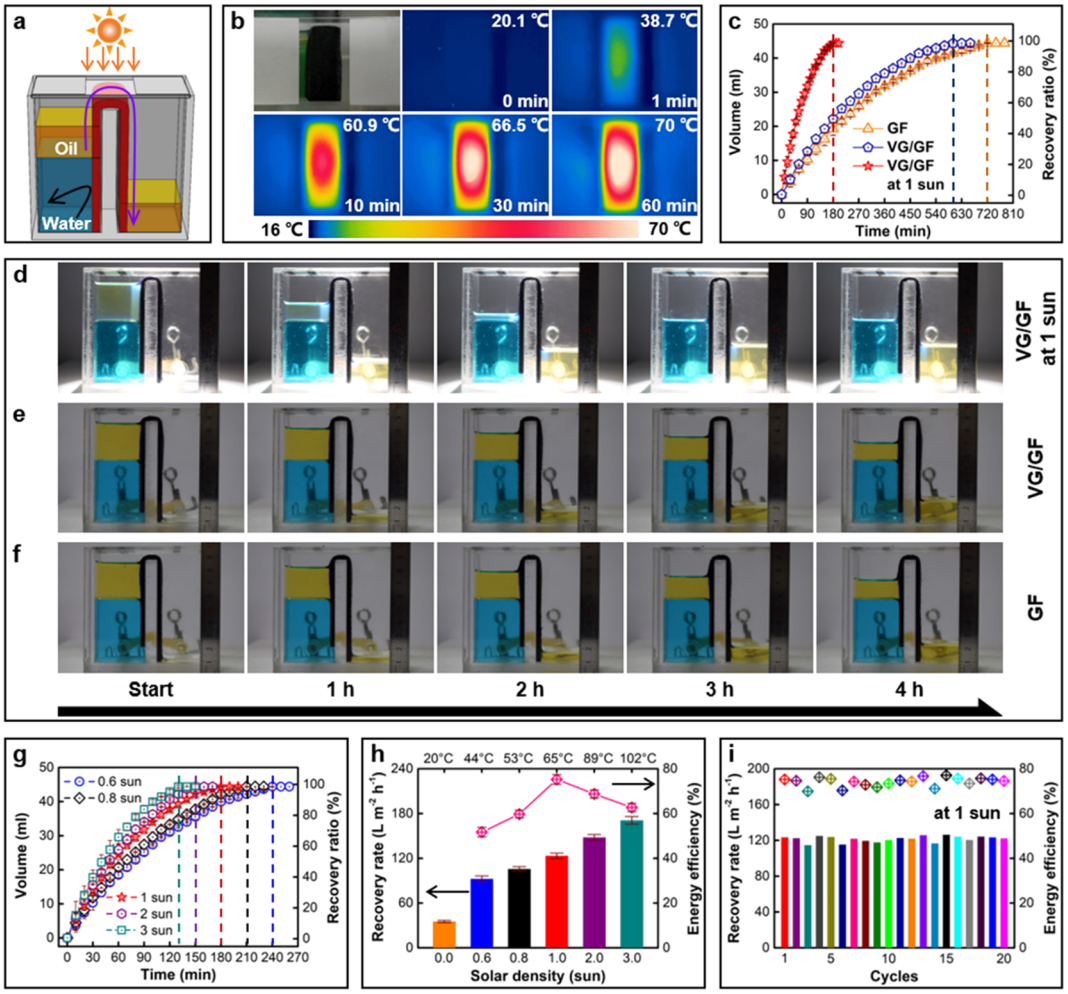

Figure 3. Oil collection performance of the S-SOS device. (a) Experimental setup of the S-SOS device. The blue color represents water. The yellow color represents oil that floats on water. Oil transports from the left chamber to the right chamber. (b) IR images to present the temperature distribution of the U-shape architecture when working under the irradiation of a normal solar density of 1 kW m^{-2}. (c) The volume evolutions of oil collection of the S-SOS device equipped with a pristine GF sample or a VG/GF sample. (d) Optical images of the S-SOS device equipped with a VG/GF sample under the irradiation of a normal solar density of 1 kW m^{-2}. (e) Optical images of the S-SOS device equipped with a VG/GF sample at ambient condition. (f) Optical images of the S-SOS device as the U-shape architecture pristine GF sample at ambient condition. (g) The volume evolutions of oil collection under different solar density. The S-SOS device is equipped with a VG/GF sample. (h) Average transport rates of oil collection and solar-oil energy efficiencies under different solar density. The S-SOS device is equipped with a VG/GF sample. (i) Cyclic behavior of the S-SOS device equipped with a VG/GF sample.

contact with the surface of VG/GF, it quickly permeates into the sample, suggesting the oleophilic nature (see Figure 2f). When a water droplet contacts the surface of VG/GF, it maintains a large contact angle of 142.5°, indicating the hydrophobic feature (see Figure 2g). Such an oleophilic and hydrophobic surface can be attributed to the following two factors. First, the all-carbon structures. The VGs are synthesized from a precursor of a hydrogen−methane gas mixture in an energy-intensive, high-temperature, and high-vacuum environment. As such, the VGs are composed of high-purity carbon hexagonal lattices. As shown by the X-ray photoelectron spectroscopy (XPS) result in Figure S5, only carbon-associated peaks can be observed. Oleophobic surface groups (e.g., fluorine-containing functional groups[27,28]) and hydrophilic surface groups (e.g., oxygen-containing functional groups that often occur in reduced graphene oxides fabricated by chemical methods[29,30]) do not exist in the VG/GF material. Meanwhile, all-carbon materials often show a good affinity with organic liquids, such as oil. Thus, the VG/GF is intrinsically oleophilic and hydrophobic. Second, the rough surface. According to Wenzel relation ($\cos\theta^* = r\cos\theta$, where θ^* is the contact angle on a rough surface, θ is the contact angle on a smooth surface, and r is roughness factor. $r = 1$ if the surface is smooth; $r > 1$ if the surface is rough), a surface wettability can be enhanced by increasing the surface roughness.[31] As shown in Figure 2 and Figure S2, VGs are uniformly coated on the surface of carbon fibers, changing the surface from smooth to highly rough. On such a rough surface, the surface wettability will be improved. The hydrophobic wettability become more hydrophobic, where the water contact angle increases from 128.7° to 142.5° after the VG coating (see Figure S6). Yet, it is hard to quantify the change of oleophilic nature after VG coating because the oil contact angle of the GF sample is also measured to be 0°.

Light absorption is an important property to determine the ability to harvest solar energy. The photonic reflectance (R) and transmittance (T) of the VG/GF sample (with a thickness of 5 mm) are experimentally measured. The photonic

DOI: 10.1021/acsnano.9b05703
ACS Nano 2019, 13, 13027−13036

absorbance (A) is calculated by the equation ($A = 1 - R - T$). As shown in Figure 2h, the VG/GF sample displays high light absorption over a wide wavelength range from 200 to 2600 nm, which covers the most energetic part of the solar spectrum (*i.e.*, the ultraviolet−visible−near-infrared region). The light absorbance is calculated to be 98.1%, indicating that less than ∼2% of light reflects from or transmits through the VG/GF sample. For comparison, the light absorbance of a pristine GF sample is measured to be 88.4% (see Figure S7), much lower than that of the VG/GF sample. It is suggested that VG coating can improve the light absorption. Such a high light absorptance can be attributed to VGs' vertical orientation and cavity structures.[24,32−34] First, the optical property of graphene is highly associated with its orientation, which was studied in detail in our prior works.[24,34] The photonic absorption coefficient along the orientation parallel to the graphene plane is 1−2 orders of magnitude greater than that of the orientation perpendicular to the graphene plane within the ultraviolet−visible−near-infrared region. It is because the imaginary part of the dielectric functions, which is highly associated with optical property, along the graphene in-plane orientation could be 1−2 orders of magnitude larger than that of the graphene cross-plane orientation.[24] The VGs with the orientation nearly parallel to the incident light can maximize their ability to harvest solar energy. Apart from the vertical orientation, the open channels and dense arrays of the VGs can trap the incident light like a hohlraum. After multiple internal reflections in these cavity structures, the incident light is almost completely absorbed by the graphene nanostructures, leading to the high light absorption.[34,35]

In practical applications, the S-SOS device might work under a variety of weather conditions, such as storm and scorching heat. Such harsh working-conditions require the VG/GF material to be thermally and mechanically stable. As shown in Figure 2i, the thermogravimetry curves of the VG/GF sample were obtained when the sample was exposed to a simulated air flow (O_2/N_2 = 2:8). The weight of the VG/GF sample is well maintained until the temperature increases to ∼500 °C. The highest temperature achieved in the current work is 102.2 °C under the irradiation of a high solar density of 3 kW m^{-2}, which is far lower than the degradation temperature of ∼500 °C. On the other hand, mechanical property tests of the VG/GF sample, including a tensile test and a cyclic compressive test, were conducted. As shown by the result of the tensile test (see the red line) in Figure 2j, the ultimate tensile strain of the VG/GF sample reaches 21.5% with a maximum tensile stress of 0.324 MPa. As shown by the result of the cyclic compressive test in Figure 2j, the VG/GF presents an elastic deformation under the maximum compressive strain of 50%. The cyclic curves from the second cycle to the tenth cycle nearly overlap with a negligible degradation of stress during the loading−unloading processes, while an obvious decline from the first cycle to the second cycle is observed. The decline in the first cycle is possibly caused by the exhaust of the air that initially fills the interspace of the GF frameworks. The outstanding recoverability from the second to the tenth cycle can be explained by the cross-linked carbon-fiber structures. Therefore, the VG/GF material is thermally stable and mechanically robust to endure harsh conditions and long-term operation

Oil Recovery Performance. As schematically shown in Figure 3a, the lab-scale S-SOS prototype is assembled by two chambers, which are separated by a wall. The left chamber is used to simulate the ocean on which oil is floating, while the right chamber is used to collect and store the oil. The VG/GA sample with a thickness of 5 mm and a width of 40 mm (corresponding to a projected cross-sectional area of 40 × 5 mm^2) covers the separating wall to serve as the inverted U-shape architecture. A solar simulating source is employed to illuminate the S-SOS device from the top. To eliminate the influence of solar irradiation on the floating oil in the chambers, the light is only allowed to illuminate the top surface of the VG/GA sample, while the light upon two chambers is blocked. During the oil recovery test, the water is poured into the left chamber, as shown by Video S1, then the oil is poured into the left chamber, and immediately the oil recovery process begins. As shown by the left test in Video S1, the oil spontaneously flows from the left to the right through the U-shape architecture at ambient environment. When the light is turned on, the speed of oil recovery is dramatically increased, as shown by the right test in Video S1.

When exposed to irradiation, the VG/GF sample harvests solar energy and converts it to thermal energy, causing the increased surface temperature. As shown by the infrared (IR) images in Figure 3b, under the irradiation with a normal solar density of 1 kW m^{-2}, the surface temperature of the VG/GF sample quickly increases from room temperature (20.1 °C) to 38.7 °C within 1 min, then slowly increases and eventually reaches a plateau of ∼70 °C. When oil transports through the hot U-shape architecture, it is heated via interfacial heating to obtain a high temperature close to 70 °C (see the oil temperature evolution curves recorded by thermocouples in supporting section 8).

The oil volume that is collected in the right chamber is recorded by a digital camera and shown in Figure 3c−f. When the solar simulator is turned off, the oil recovery process can be completed within ∼600 min (Figure 3e), corresponding to an average oil-recovery rate of 35.2 L m^{-2} h^{-1} flowing through the cross-sectional area (40 × 5 mm^2) of the VG/GF sample. Almost 100% of the oil that floats on the water surface is recovered, as shown by Video S1. When the solar simulator is turned on, the oil recovery process is dramatically increased. Under the solar irradiation of 1 kW m^{-2}, the oil recovery process can complete within ∼180 min, as shown in Figure 3d. Correspondingly, the oil-recovery rate is calculated to be 123.3 L m^{-2} h^{-1}, which is 3.5 times higher than without solar lighting (35.2 L m^{-2} h^{-1}). The increase of the oil-recovery rate is mainly caused by the solar-heating effect that makes a significant influence on the oil viscosity and the flow resistance. This point will be discussed in detail in the following section.

For comparison, an oil recovery test using a pristine GF sample as the U-shape architecture was also conducted (see the left test in Video S2). As shown by Figure 3c−f, the oil recovery process is completed in ∼720 min, which is longer than that of the VG/GF sample (∼600 min). The result suggests that coating VGs on the frameworks of GF can accelerate the recovery process. Such an improvement can be attributed to the nanostructure-enhanced siphon and capillary actions, which will be discussed in details in the following section.

In practical applications, the intensity of solar irradiation is unstable by nature, which may make significant influences on the oil recovery performance. Besides, solar concentrators are often used in some cases. For this consideration, we have conducted a series of oil recovery tests under different solar irradiation densities ranging from 0.6 sun to 3 sun. As shown in Figure 3g, the total time spent for oil recovery process is

DOI: 10.1021/acsnano.9b05703
ACS Nano 2019, 13, 13027−13036

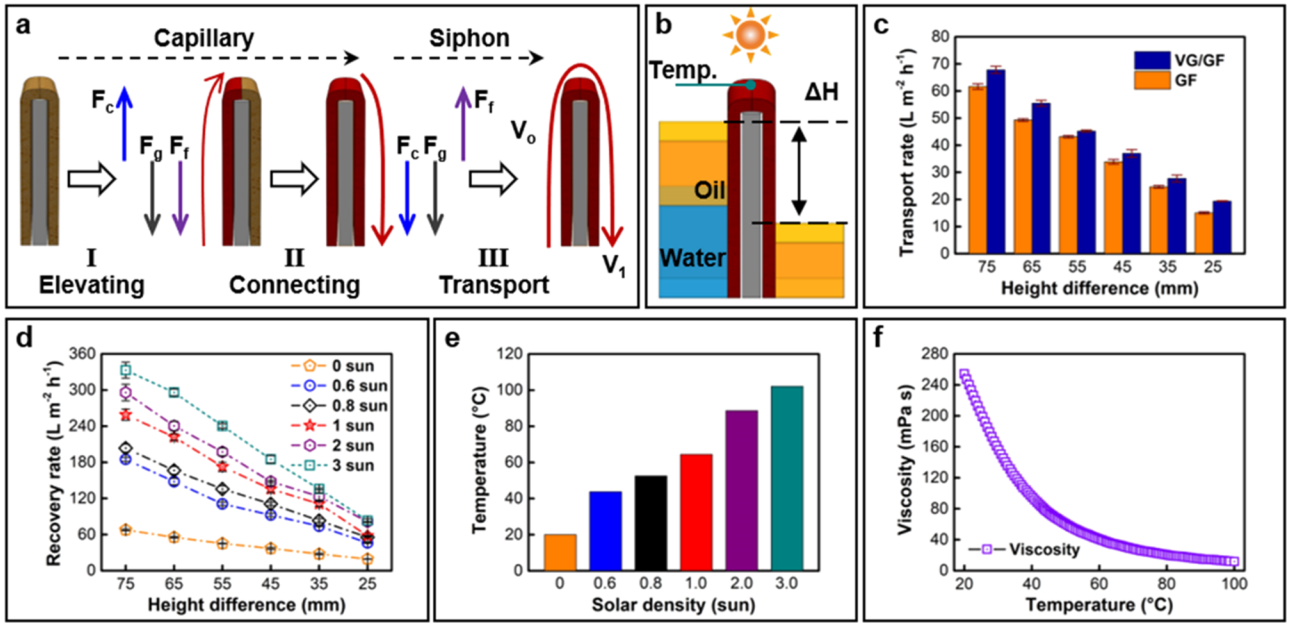

Figure 4. Mechanism demonstration of the S-SOS device. (a) Illustration of the siphon capillary oil transport process. The analysis of force balance is available in supporting section 10. (b) Schematic of the experimental setup for height difference (ΔH). (c) Comparison of the average transport rates of the S-SOS device under different height differences. (d) Comparison of the average transport rates of the S-SOS device under different solar densities. (e) Oil temperature at the top point (see panel b) of the U-shape architecture under different solar densities. (f) The evolution of the oil viscosity at different temperatures.

reduced from ~240 to ~130 min, when the solar density increases from 0.6 to 3 sun. Correspondingly, the average transport rates of the whole oil recovery process are calculated to be 92.5, 105.7, 123.3, 148, and 170.8 L m^{-2} h^{-1} at 0.6, 0.8, 1, 2, and 3 sun, respectively. Apparently, the average oil-recovery rate increases proportionally with the solar density.

The incident solar energy is harvested by the VG/GF sample and then converted into thermal energy, which is used to locally heat the oil flowing in the VG/GF structures. As such, the solar-thermal energy efficiency ($\eta_{\text{solar-thermal}}$), defined as the percentage of the incident solar energy used to heat the oil, can be calculated by the following equation:

$$\eta_{\text{solar-thermal}} = V\rho C(T - T_o)/Q_{\text{solar}} \quad (1)$$

where V is oil volume transport rate flowing through the projected cross-sectional area of the VG/GF sample, ρ is the mass density of oil (which varies with temperature, as shown in Figure S10), C is specific heat of oil (taking 2000 J kg^{-1} K^{-1}), T is the temperature of the oil flow (measured by a thermocouple), T_0 is the initial temperature of the floating oil, and Q_{solar} is the input solar energy illuminates on the plateau of the VG/GF sample (40 × 10 mm^2 in the current work). As shown in Figure 3h, when increasing the solar density from 0.6 to 1 sun, the solar-thermal energy efficiency gradually increases from 51.7% to 75.3%. However, when further increasing the solar energy to 2 sun and 3 sun, the energy efficiency decreases to 68.8% and 62.7%, respectively. It is worth noting that the maximum solar-thermal energy efficiency occurs at 1 sun. This phenomenon is associated with the oil viscosity evolution with the oil temperature. Detailed discussion will be provided in next section.

Moreover, a cyclic test with 20 cycles was conducted at 1 sun to detect the stability of the VG/GF sample. As shown in Figure 3i, the oil-recovery rates range from 110 to 130 L m^{-2} h^{-1}. Correspondingly, the solar-thermal energy efficiency is calculated to be 74.1 ± 2.1% with a small fluctuation, and no noticeable performance degradation is observed during the ~60 h of operation. The excellent performance and long-term stability can be ascribed to the following factors. First, the superior ability to harvest light across a wide wavelength. More than 98% of incident light is captured by the VG/GF sample due to the VGs' vertical orientation, wall-like arrays, and exposed edges. Second, the fin-like VGs (see Figure 2e) can increase the contacting area with oil. Meanwhile, the oleophilic surface leads to a good affinity between VGs and oil. As such, the heat generated in VGs by solar-thermal conversion can transfer through the VGs/oil interface efficiently. As shown by the IR images in Figure 3b and the oil temperature curves in Figure S9, the oil can gain a temperature (~65 °C) that is very close to VGs' surface temperature (~70 °C). Third, the thermal and mechanical stability also contributes to the stable performance over such a long-time operation.

Fluid Transport Mechanism. The oil recovery process by the S-SOS device can be principally divided into three stages: (i) elevating, (ii) connecting, and (iii) transporting, as shown in Figure 4a. Particularly, stage i and stage ii are associated with the capillary action, while stage iii is related to the siphon action.

As shown in Figure 4a,I, at stage i, oil permeates into the VG/GF sample and flows upward above the oil surface. The oil is pulled by capillary force (F_c) against gravity (F_g) and flow resistance (F_f). At this stage, the solid surface energy (E_σ^s) is reduced during the capillary wetting process. According to *Sophocleous*'s report,[36] the surface energy difference (ΔE_σ^s) can be calculated as

$$\Delta E_\sigma^s = A_{s\text{-}l}(\sigma_{s\text{-}v} - \sigma_{s\text{-}l}) \quad (2)$$

where $A_{s\text{-}l}$ is the solid−liquid interfacial area, $\sigma_{s\text{-}l}$ is the solid−liquid interfacial surface tension, and $\sigma_{s\text{-}v}$ is solid−air interfacial

DOI: 10.1021/acsnano.9b05703
ACS Nano 2019, 13, 13027−13036

surface tension. The surface energy difference is used to overcome the gravity and flow resistance, driving the oil to rise.

As shown in Figure 4a,II, at stage ii, oil flows downward and fills the porosity of the VG/GF sample. The two chambers are connected by the oil flow existing in the inverted U-shape architecture. At this stage, the oil is pulled by capillary and gravity force against flow resistance. The surface energy difference (ΔE_σ^s) and the gravitational potential energy difference ($\Delta E_g = mg\Delta h$, where Δh is height change of liquid) are used to overcome the flow resistance, driving the oil to flow downward.

As shown in Figure 4a,III, at stage iii, oil continuously flows through the inverted U-shape architecture, and then discharges at the right chamber (*i.e.*, downstream). Based on *Bernoulli's* relation,[21] the flow velocity at downstream (V) can be derived by

$$V = [2(g\Delta H - \Delta P_f/\rho)]^{1/2} \quad (3)$$

where g is gravitational acceleration, ΔH is the height difference between the upstream and the downstream, ΔP_f is the total pressure drop caused by flow resistance, respectively. As such, the flow velocity is mainly determined by the height difference and the flow resistance. The gravitational potential energy difference (ΔE_g) is used to overcome the flow resistance, driving the oil flow.

Nanostructure-Enhanced Fluid Transport. Figure 3c and Video S2 have shown that the VG coating can accelerate the oil recovery process. Here, the oil recover performance of the VG/GF sample and of a pristine GF sample is systematically compared, as shown in Figure 4b,c. On one hand, the oil-recovery rate decreases when the height difference (ΔH) is reduced from 75 to 25 mm because a larger height difference leads to a faster oil flow velocity. On the other hand, at same height difference, the VG/GF sample shows a higher oil-recovery rate compared with the GF sample. Such an improvement can be attributed to the abundant channels built by the plasma-made graphene nanostructures. According to the *Laplace–Young* equation,[37] the capillary force (F_c) is determined by the effective pore radius (r) of the transporting channel, the liquid surface tension (σ), and the liquid–solid contact angle (θ):

$$F_c = A \times \Delta P_c = A \times 2\sigma \cos\theta/r \quad (4)$$

where A is assumed to be the projected cross-sectional area of the transport channel and ΔP_c is capillary pressure. Since the capillary force increases inversely with the pore radius of the transport channel, a smaller channel will lead to a larger capillary force to pull fluid transport. The graphene nanostructures with a typical height of 1–5 μm are much smaller than the pore size of the hosting structure (tens to hundreds of micrometers). These wall-like VGs build open and interconnected channels (see Figure 2). The size of the as-obtained graphene channels ranges from hundreds of nanometers to tens of micrometers. When fluids flow through the smaller channels, the capillary force is dramatically increased, and thus accelerates the oil recovery.

In addition, based on *Young's* equation ($\sigma_{s\text{-}v} - \sigma_{s\text{-}l} = \sigma_{l\text{-}v}\cos\theta$) and *Sophocleous's* equation ($\Delta E_\sigma^s = A_{s\text{-}l}(\sigma_{s\text{-}v} - \sigma_{s\text{-}l})$),[38] the amount of surface energy consumed for capillary adsorption is associated with the liquid–air surface tension ($\sigma_{l\text{-}v}$) and the liquid–solid contact angle (θ). The $\sigma_{l\text{-}v}$ is temperature-dependent, as shown in Figure S11. A smaller θ leads to a higher harvest of the solid surface energy to drive the oil recovery. As shown in Figure 2f, the oil contact angle is measured to be 0°, indicating the high harvest of solid surface energy. It is worth noting that the oil contact angle of a GF sample is also measured to be 0°, as shown in Figure S6. When liquid completely spreads on the solid surface (*i.e.*, the contact angle equals to zero), the surface energy difference calculated by the *Sophocleous's* equation will be inaccurate.[38] As such, it is still difficult to determine the superiority of the VG/GF over the GF sample on harvesting solid surface energy.

Solar-Heating-Enhanced Fluid Transport. Figure 3c and Video S1 have shown that solar irradiation can also increase the oil recovery rate. The oil recovery performance under different solar density is studied. As shown in Figure 4d, the recovery rate increases proportionally with the solar density under the same height difference. It is suggested that solar irradiation has a significant influence on the oil recovery process. As mentioned before, flow resistance (F_f) plays a crucial role on the siphon transport process. According to *Darcy's* law,[39] the flow resistance can be derived by

$$F_f = A \times \Delta P_f = A \times 4\eta l u/(r^2\varepsilon) \quad (5)$$

where η is viscosity, l is the flow distance, u is velocity, and ε is the porosity of the porous material. The oil flow in the VG channels is assumed to be a fully developed laminar fluid.[40] The A, l, ε, and r are considered as constants because they are related to the morphologic and structural features of the VG/GF sample. Thus, the flow resistance is mainly determined by the oil viscosity and oil flow velocity. By decreasing the oil viscosity, the flow resistance can be reduced.

When exposed to solar irradiation, the surface temperature of the VG/GF sample increases and then heats the oil flow. As shown in Figure 4b, a thermocouple was applied to measure the oil temperature at the plateau. The room temperature maintains at 20 °C. The results are presented in Figure 4e. When exposed to 0.6 sun, 0.8 sun, 1 sun, 2 sun, and 3 sun, the oil temperature is measured to be 43.8, 52.6, 64.5, 88.7, and 102.1 °C, respectively. Then, the oil viscosity ranging from 20 to 100 °C was measured as shown in Figure 4f. A sharp reduction from 254.2 to 40.6 mPa s is observed when the oil temperature increases from 20 to 60 °C. When continuously increasing the temperature from 60 °C, the oil viscosity decreases slowly, leading to a small change of 28.8 mPa s from 60 to 100 °C. Such an oil viscosity evolution can be used to explain why the maximum energy efficiency occurs at 1 sun. When the solar density increases from 0.6 sun to 1 sun, the oil temperature increases from 43.8 to 64.5 °C. The oil viscosity reduces from 79.0 to 33.7 mPa s, leading to a relatively large increase of the oil-recovery rate from 92.5 to 123.3 L m^{-2} h^{-1}. The solar–oil energy efficiency is thus increased from 51.7% to 75.3%. When the solar density is further increased to 2 sun, although the oil temperature increases to 88.7 °C, only a small reduction of the oil viscosity of 8.9 mPa s is obtained. The oil-recovery rate increases from 123.3 to 148.0 L m^{-2} h^{-1} with a small rise of 20% while the solar density increases by 2-fold. It causes the decline of the solar-thermal energy efficiency to 68.8%. Similarly, when increasing the solar density from 2 sun to 3 sun, the solar-thermal energy efficiency decreases to 62.7%. More information, including the evolution of the oil recovery rate as functions of solar density, oil temperature, and oil viscosity, is available in Figure S12. It is worth noting that the optimum value of solar density varies with solar-thermal materials and oil species.

DOI: 10.1021/acsnano.9b05703
ACS Nano 2019, 13, 13027–13036

The oil recovery rate up to 170.8 L m^{-2} h^{-1} is lower than the previous work (580 L m^{-2} h^{-1}) that involved electricity-powered pumping.[41] Nevertheless, the slow recovery can be mitigated by the advantages in terms of economic and energetic costs for the oil recovery process. In the previous reports, complex devices, such as electrical pumps, squeezers, centrifuges, and heaters were equipped to drive the oil recovery process, as shown in Table S1. Despite the relatively high recovery rate, the cost for the oil recovery process was also high, not to mention the expenses of these electrical devices. In contrast, the current S-SOS device utilizes energy all from nature, including solid surface energy, gravitational potential energy, and solar energy, to drive the oil recovery process. It does not require power input (e.g., electricity) or a complex device (e.g., electrical pump), and can be simply achieved by an inverted U-shape architecture. As a result, the total cost for oil recovery is reduced. Detailed comparison between the current S-SOS and the previous oil recovery devices is available in supporting section 13. It is worth noting that the plasma-made VGs are crucial to the oil recovery performance of the S-SOS device, which is summarized in Table S2. In addition, future works can focus on increasing the height difference and optimizing the size of the transport channels to improve the oil recovery rate. More importantly, such a self-pumping mechanism can be also applied to other fluid transport applications, such as the separation of organic liquid and water, and the separation of particles and liquid.

Economic Analysis. Ocean oil spill accidents severely damage marine ecosystems and cause great losses of valuable resources. For instance, during the Gulf of Mexico oil spill accident in 2010, an estimated amount of ~4.9 million barrels of oil leaked to the ocean.[42] Despite huge multinational remediation efforts and the use of ~1.84 million gallons of dispersants, thick layers of oil cover ocean surfaces for decades.[43,44] Therefore, environment-friendly and economically efficient solutions are essential. We assume that the S-SOS device in the current work is employed and assembled on a marine vessel to clean up the oil spill, as shown in Figure 1a. The carrying-capacity of the vessel is assumed to be 1000 tonnes, which usually has a length of 30 to 50 m and a height of 5 to 10 m. We assume two gunnels with 30 m length and 5 m height are covered by the VG/GF material (with a thickness of 0.1 m), costing $139,200 with a material volume of 60 m^3. The projected cross-sectional area of the transport channel is calculated to be 6 m^2. If the S-SOS device works for a year (e.g., 365 days with alternations of 12 h daylight and 12 h night, where the average solar density on daylight is assumed to be 0.6 sun), the amount of oil recovered is expected to be 21 265 barrels, corresponding to an economic benefit of $1,275,900 and an annual return of up to ~817% (assuming the cost of $60 per barrel of oil). Note that the analysis ignores the performance deterioration at a large scale, harsh weather, and ocean waves, *etc.* Importantly, the S-SOS devices operate in a self-pumping and manual-intervention-free manner and do not affect other working components on the vessel.

CONCLUSIONS

High economic and energetic costs caused by a complex process remain significant challenges in oil spill recovery. This work proposes an S-SOS design to enable the efficient oil cleanup and recovery in a self-pumping manner. The current S-SOS device is simply assembled by an inverted U-shaped porous architecture, which can harvest surface energy, gravitational potential energy, and solar energy to drive the oil recovery while no external power input and no manual intervention are needed. In the current proof-of-concept work, an all-carbon hierarchical architecture (*i.e.*, VG/GF) is fabricated by growing VGs on a monolith of GF through a one-step PECVD method to serve as the U-shape architecture, leading to the enhanced siphon action, capillary action, photonic absorption, and interfacial heating in the plasma-made graphene nanostructures.

During the oil recovery tests, the oil-recovery rate at the VG/GF reaches 35.2 L m^{-2} h^{-1}, which is higher than that at a pristine GF (30.8 L m^{-2} h^{-1}). The improvement is ascribed to the nanostructure-enhanced capillary action. Moreover, by heating the U-shape architecture through solar-thermal conversion, the oil-recovery rate dramatically increases. The average transport rates of the whole oil recovery process are calculated to be 92.5, 105.7, 123.3, 148, and 170.8 L m^{-2} h^{-1} at 0.6, 0.8, 1, 2, and 3 sun, respectively. The improvement is attributed to the decreased oil viscosity and the reduced flow resistance under irradiation. The maximum energy efficiency of 75.3% occurs at 1 sun, which is related to the oil viscosity evolution under irradiation. Additionally, the VG/GF structure presents an excellent long-term stability over 60 h of operation duration. The stable performance with high oil-recovery rate and high energy efficiency is ascribed to the nanostructure-enhanced oil-transport behavior, superior light absorption, enhanced interfacial heating as well as the thermal and mechanical stability. Multiple merits including self-pumping, nanostructure- and solar-enhanced siphon and capillary actions as well as efficient energy utilization make the current S-SOS design and the VG/GF nanostructures promising for oil spill recovery and other fluid transport applications.

METHODS

Material Fabrication. The commercially available GF (with a thickness of 5 mm, $10 m^{-2}) was used as the hosting structure of VGs. The VGs were synthesized by a customized inductively coupled plasma enhanced chemical vapor deposition (ICP-PECVD) system. In a typical procedure, a monolith of GF with a plane size of 4 cm × 20 cm was placed in a sealed cylindrical quartz tube, vacuumed to <10 Pa, and heated to 700 °C. A gas flow of CH_4 (5 mL min^{-1}) and H_2 (5 mL min^{-1}) was injected into sealed tubes to act as precursors. The growth pressure was maintained at ~100 Pa. Subsequently, a radio frequency source of 250 W was coupled into the quartz tube. After 1 h synthesis, the sample was cooled down under the protection of 10 mL min^{-1} Ar flow to obtain the VG/GF sample. The cost for the PECVD growth is estimated to be $1.6 m^{-2}. The density of the obtained VG/GF is measured to be 0.2 g cm^{-3}.

Materials Characterization. Scanning electron microscope (SU-70, Hitachi) and transmission electron microscope (JEM 2100F, JEOL) were applied to characterize the morphology of the samples. An ultraviolet−visible−near-infrared spectrophotometer (UV-3150, Shimadzu) was used to measure the photonic transmittance (T) and reflectance (R), in which an integrating sphere was used. Photonic absorbance (A) was calculated by $A = 1 - T - R$. The X-ray photoelectron spectroscope (Escalab Mark II, VG) with a monochromatic Mg Ka X-ray source (1,253.6 eV) was employed to measure the elemental compositions. Thermogravimetry analysis was conducted under simulated air flow (O_2/N_2 = 1:4) from 50−700 °C (Q500, TA). The mechanical properties were measured by a universal material testing machine (Roell Z020, Zwick). The structural porosities were measured by a mercury porosimeter (AutoPore IV 9510, Micromeritics). The oil viscosity was measured by a rotary rheometer (RS6000, HAAKE).

Oil Recovery Test. During the oil recovery tests, 48 mL of mineral oil and 80 mL of deionized water were poured into the left

DOI: 10.1021/acsnano.9b05703
ACS Nano 2019, 13, 13027−13036

chamber. The oil recovery process is recovery by a digital camera (Nikon D5300). A solar simulator (PLS-SXE300D, Beijing Perfect Light Technology) with a <5° collimated output was used as the light source. An optical filter was used to obtain a standard AM 1.5G spectrum. An optical power meter (PL-MW2000, Beijing Perfect Light Technology) was used to detect the solar density. Four T-type thermocouples (with an accuracy of 0.01 °C) were inserted into the VG/GF sample to measure the oil temperature. An infrared camera (T1050sc, FLIR) was used to detect the surface temperature distribution of the VG/GF sample. The oil-recovery rate was calculated based on the projected cross-sectional area (*i.e.*, 40 × 5 mm^2 in the current work). All tests were conducted at ambient temperature of ∼20 °C and atmospheric pressure of ∼0.1 MPa, with a humidity of ∼48%. Error analysis is conducted with multiple sets of repeatable tests.

ASSOCIATED CONTENT

Supporting Information

The Supporting Information is available free of charge on the ACS Publications website at DOI: 10.1021/acsnano.9b05703.

Comparison between the current S-SOS device and conventional oil recovery devices; concept and operation; morphology of the pristine GF sample; plasma growth mechanism; XPS spectrum of VG/GF; wetting behavior of the pristine GF sample; comparison of photonic absorbance between VG/GF and bare GF; temperature evolution during the oil recovery process; mass density of oil as a function of temperature; analysis of force balance; surface tension of oil as a function of temperature; recovery rate evolution; comparison of the current S-SOS and the previous oil recovery devices; crucial roles of VGs (PDF)

Accelerated (720×) video of the nanostructure-enhanced oil recovery (MP4)

Accelerated (720×) video of the solar-heating-enhanced oil recovery (MP4)

AUTHOR INFORMATION

Corresponding Author

*E-mail: bozh@zju.edu.cn.

ORCID

Tengfei Luo: 0000-0003-3940-8786

Timothy S. Fisher: 0000-0002-8909-313X

Zheng Bo: 0000-0001-9308-7624

Kostya Ken Ostrikov: 0000-0001-8672-9297

Author Contributions

#S.W., H.Y., and G.X. contributed equally to this work. Z.B., S.W., and K.(K.)O., conceived the project. H.Y., G.X., and T.L. discussed with Z.B., S.W., and K.(K.)O. on the conceptualization of the work and experimental designs. Z.B., S.W., H.Y., B.G., and Y.T. fabricated materials and performed experiments. S.W., H.Y., G.X., T.L., and T.F. performed theoretical analysis. Z.B., S.W., H.Y., G.X., T.L., T.F., J.Y., K.C., and K.(K.)O. analyzed the data and interpreted the results. All the authors contributed to the writing of the manuscript.

Notes

The authors declare no competing financial interest.

ACKNOWLEDGMENTS

This work is supported by the National Natural Science Foundation of China (Grant No. 51576175) and Zhejiang Provincial Natural Science Foundation of China (Grant No. LR17E060002). Z.B. thanks the National Program for Support of Top-notch Young Professionals. G.X. would like to acknowledge the financial support by the start-up funding from the University of Nevada, Reno. K.(K.)O. thanks the Australian Research Council for partial support. T.L. thanks the support from National Science Foundation (Grant No. 1706039).

REFERENCES

(1) Whitfield, J. How to Clean a Beach. *Nature* **2003**, *422*, 464−466.

(2) Jernelov, A. How to Defend against Future Oil Spills. *Nature* **2010**, *466*, 182−183.

(3) Ma, Q.; Cheng, H.; Fane, A. G.; Wang, R.; Zhang, H. Recent Development of Advanced Materials with Special Wettability for Selective Oil/Water Separation. *Small* **2016**, *12*, 2186−2202.

(4) Ge, J.; Zhao, H.-Y.; Zhu, H.-W.; Huang, J.; Shi, L.-A.; Yu, S.-H. Advanced Sorbents for Oil-Spill Cleanup: Recent Advances and Future Perspectives. *Adv. Mater.* **2016**, *28*, 10459−10490.

(5) Ge, M.; Cao, C.; Huang, J.; Zhang, X.; Tang, Y.; Zhou, X.; Zhang, K.; Chen, Z.; Lai, Y. Rational Design of Materials Interface at Nanoscale Towards Intelligent Oil-Water Separation. *Nanoscale Horiz* **2018**, *3*, 235−260.

(6) Wu, M.; Shi, Y.; Chang, J.; Li, R.; Ong, C.; Wang, P. Sunlight Induced Rapid Oil Absorption and Passive Room-Temperature Release: An Effective Solution toward Heavy Oil Spill Cleanup. *Adv. Mater. Interfaces* **2018**, *5*, 1800412.

(7) Zhu, Q.; Chu, Y.; Wang, Z.; Chen, N.; Lin, L.; Liu, F.; Pan, Q. Robust Superhydrophobic Polyurethane Sponge as a Highly Reusable Oil-Absorption Material. *J. Mater. Chem. A* **2013**, *1*, 5386−5393.

(8) Li, J.; Xu, C.; Zhang, Y.; Wang, R.; Zha, F.; She, H. Robust Superhydrophobic Attapulgite Coated Polyurethane Sponge for Efficient Immiscible Oil/Water Mixture and Emulsion Separation. *J. Mater. Chem. A* **2016**, *4*, 15546−15553.

(9) Ge, J.; Shi, L.-A.; Wang, Y.-C.; Zhao, H.-Y.; Yao, H.-B.; Zhu, Y.-B.; Zhang, Y.; Zhu, H.-W.; Wu, H.-A.; Yu, S.-H. Joule-Heated Graphene-Wrapped Sponge Enables Fast Clean-Up of Viscous Crude-Oil Spill. *Nat. Nanotechnol.* **2017**, *12*, 434−440.

(10) Ge, J.; Ye, Y.-D.; Yao, H.-B.; Zhu, X.; Wang, X.; Wu, L.; Wang, J.-L.; Ding, H.; Yong, N.; He, L.-H.; Yu, S.-H. Pumping through Porous Hydrophobic/Oleophilic Materials: An Alternative Technology for Oil Spill Remediation. *Angew. Chem., Int. Ed.* **2014**, *53*, 3612−3616.

(11) Wang, Y.; Zhou, L.; Luo, X.; Zhang, Y.; Sun, J.; Ning, X.; Yuan, Y. Solar-Heated Graphene Sponge for High-Efficiency Clean-Up of Viscous Crude Oil Spill. *J. Cleaner Prod.* **2019**, *230*, 995−1002.

(12) Jiang, Z.-R.; Ge, J.; Zhou, Y.-X.; Wang, Z. U.; Chen, D.; Yu, S.-H.; Jiang, H.-L. Coating Sponge with a Hydrophobic Porous Coordination Polymer Containing a Low-Energy CF_3-Decorated Surface for Continuous Pumping Recovery of an Oil Spill from Water. *NPG Asia Mater.* **2016**, *8*, No. e253.

(13) Zhang, L.; Li, H.; Lai, X.; Su, X.; Liang, T.; Zeng, X. Thiolated Graphene-Based Superhydrophobic Sponges for Oil-Water Separation. *Chem. Eng. J.* **2017**, *316*, 736−743.

(14) Luo, Y.; Jiang, S.; Xiao, Q.; Chen, C.; Li, B. Highly Reusable and Superhydrophobic Spongy Graphene Aerogels for Efficient Oil/Water Separation. *Sci. Rep.* **2017**, *7*, 7162.

(15) Boatwright, A.; Hughes, S.; Barry, J. The Height Limit of a Siphon. *Sci. Rep.* **2015**, *5*, 16790.

(16) Jean, J.-S. Pumping Testing Using a Siphon Well. *Water Resour. Manage.* **1996**, *10*, 81−105.

(17) Wichelns, D.; Houston, L.; Cone, D. Economic Analysis of Sprinkler and Siphon Tube Irrigation Systems, with Implications for Public Policies. *Agr. Water Manage.* **1997**, *32*, 259−273.

(18) Tadayon, R.; Ramamurthy, A. S. Discharge Coefficient for Siphon Spillways. *J. Irrig. Drain. Eng.* **2013**, *139*, 267−270.

(19) Zhao, Y.; Su, Y.; Chen, G.; Yuan, Q. Effect of Surface Properties on the Flow Characteristics and Mass Transfer Performance in Microchannels. *Chem. Eng. Sci.* **2010**, *65*, 1563−1570.

DOI: 10.1021/acsnano.9b05703
ACS Nano 2019, 13, 13027−13036

(20) Cai, Y.-L.; Sun, H.-Y.; Shang, Y.-Q.; Wu, Z.-J. Air Accumulation in High-Lift Siphon Hoses under the Influence of Air Dissolution and Diffusion. *J. Zhejiang Univ., Sci., A* **2015**, *16*, 760−768.
(21) Jeong, G. S.; Oh, J.; Kim, S. B.; Dokmeci, M. R.; Bae, H.; Leede, S.-H.; Khademhosseini, A. Siphon-Driven Microfluidic Passive Pump with a Yarn Flow Resistance Controller. *Lab Chip* **2014**, *14*, 4213−4219.
(22) Guo, Z.; Cao, Y. D. Experimental Studies of Biliquid Capillary Siphons. *Chem. Eng. Sci.* **2005**, *60*, 2621−2626.
(23) Jussila, M.; Palonen, S.; Porras, S. P.; Riekkola, M. L. Compensation of the Siphoning Effect in Nonaqueous Capillary Electrophoresis by Vial Lifting. *Electrophoresis* **2000**, *21*, 586−592.
(24) Wu, S.; Xiong, G.; Yang, H.; Tian, Y.; Gong, B.; Wan, H.; Wang, Y.; Fisher, T.; Yan, J.; Cen, K.; Bo, Z.; Ostrikov, K. Scalable Production of Integrated Graphene Nanoarchitectures for Ultrafast Solar-Thermal Conversion and Vapor Generation. *Matter* **2019**, *1*, 1017−1032.
(25) Yu, K.; Lu, G.; Bo, Z.; Mao, S.; Chen, J. Carbon Nanotube with Chemically Bonded Graphene Leaves for Electronic and Optoelectronic Applications. *J. Phys. Chem. Lett.* **2011**, *2*, 1556−1562.
(26) Wu, S.; Xiong, G.; Yang, H.; Gong, B.; Tian, Y.; Xu, C.; Wang, Y.; Fisher, T.; Yan, J.; Cen, K.; Luo, T.; Tu, X.; Bo, Z.; Ostrikov, K. Multifunctional Solar Waterways: Plasma-Enabled Self-Cleaning Nanoarchitectures for Energy-Efficient Desalination. *Adv. Energy Mater.* **2019**, *9*, 1901286.
(27) Li, F.; Wang, Z.; Huang, S.; Pan, Y.; Zhao, X. Flexible, Durable, and Unconditioned Superoleophobic/Superhydrophilic Surfaces for Controllable Transport and Oil-Water Separation. *Adv. Funct. Mater.* **2018**, *28*, 1706867.
(28) Li, F.; Bhushan, B.; Pan, Y.; Zhao, X. Bioinspired Superoleophobic/Superhydrophilic Functionalized Cotton for Efficient Separation of Immiscible Oil-Water Mixtures and Oil-Water Emulsions. *J. Colloid Interface Sci.* **2019**, *548*, 123−130.
(29) Bo, Z.; Shuai, X.; Mao, S.; Yang, H.; Qian, J.; Chen, J.; Yan, J.; Cen, K. Green Preparation of Reduced Graphene Oxide for Sensing and Energy Storage Applications. *Sci. Rep.* **2015**, *4*, 4684.
(30) Yang, J.; Pang, Y.; Huang, W.; Shaw, S. K.; Schiffbauer, J.; Pillers, M. A.; Mu, X.; Luo, S.; Zhang, T.; Huang, Y.; Li, G.; Ptasinska, S.; Lieberman, M.; Luo, T. Functionalized Graphene Enables Highly Efficient Solar Thermal Steam Generation. *ACS Nano* **2017**, *11*, 5510−5518.
(31) Quere, D. Wetting and Roughness. *Annu. Rev. Mater. Res.* **2008**, *38*, 71−99.
(32) Krivchenko, V. A.; Evlashin, S. A.; Mironovich, K. V.; Verbitskiy, N. I.; Nefedov, A.; Woell, C.; Kozmenkova, A. Y.; Suetin, N. V.; Svyakhovskiy, S. E.; Vyalikh, D. V.; Rakhimov, A. T.; Egorov, A. V.; Yashina, L. V. Carbon Nanowalls: The Next Step for Physical Manifestation of the Black Body Coating. *Sci. Rep.* **2013**, *3*, 3328.
(33) Davami, K.; Cortes, J.; Hong, N.; Bargatin, I. Vertical Graphene Sheets as a Lightweight Light Absorber. *Mater. Res. Bull.* **2016**, *74*, 226−233.
(34) Bao, H.; Kumar, A.; Cai, Y.; Ji, Y.; Fisher, T. S.; Ruan, X. Optical Properties of Thin Graphitic Nanopetal Arrays. *J. Quant. Spectrosc. Radiat. Transfer* **2015**, *158*, 84−90.
(35) Ren, H.; Tang, M.; Guan, B.; Wang, K.; Yang, J.; Wang, F.; Wang, M.; Shan, J.; Chen, Z.; Wei, D.; Peng, H.; Liu, Z. Hierarchical Graphene Foam for Efficient Omnidirectional Solar-Thermal Energy Conversion. *Adv. Mater.* **2017**, *29*, 1702590.
(36) Sophocleous, M. Understanding and Explaining Surface Tension and Capillarity: An Introduction to Fundamental Physics for Water Professionals. *Hydrogeol. J.* **2010**, *18*, 811−821.
(37) Cai, J.; Perfect, E.; Cheng, C.-L.; Hu, X. Generalized Modeling of Spontaneous Imbibition Based on Hagen-Poiseuille Flow in Tortuous Capillaries with Variably Shaped Apertures. *Langmuir* **2014**, *30*, 5142−5151.
(38) Owens, D. K.; Wendt, R. C. Estimation of the Surface Free Energy of Polymers. *J. Appl. Polym. Sci.* **1969**, *13*, 1741−1747.
(39) Shou, D.; Ye, L.; Fan, J. The Fastest Capillary Flow under Gravity. *Appl. Phys. Lett.* **2014**, *104*, 231602.
(40) Xu, P.; Yu, B. Developing a New Form of Permeability and Kozeny-Carman Constant for Homogeneous Porous Media by Means of Fractal Geometry. *Adv. Water Resour.* **2008**, *31*, 74−81.
(41) He, S.; Cheng, X.; Li, Z.; Shi, X.; Yang, H.; Zhang, H. Green and Facile Synthesis of Sponge-Reinforced Silica Aerogel and Its Pumping Application for Oil Absorption. *J. Mater. Sci.* **2016**, *51*, 1292−1301.
(42) Antonietti, M. A 'Hot' Oil Sorbent for Fast Cleanup of Viscous Crude-Oil Spills. *Natl. Sci. Rev.* **2018**, *5*, 445−446.
(43) Fragouli, D.; Athanassiou, A. Oil Spill Recovery Graphene Heaters Absorb Faster. *Nat. Nanotechnol.* **2017**, *12*, 406−407.
(44) Martinez-Palou, R.; Mosqueira, M.; Zapata-Rendon, B.; Mar-Juarez, E.; Bernal-Huicochea, C.; Clavel-Lopez, J.; Aburto, J. Transportation of Heavy and Extra-Heavy Crude Oil by Pipeline: A Review. *J. Pet. Sci. Eng.* **2011**, *75*, 274−282.

DOI: 10.1021/acsnano.9b05703
ACS Nano 2019, 13, 13027−13036